Imaging-Guided Metabolic Radiosensitization of Pediatric Rhabdoid Tumors

Wenxi Xia[a], Matthew Goff[a], Neetu Singh[a], Jiemin Huang[a], David L. Gillespie[b], Esther Need[a], Randy Jensen[b], Mark D. Pagel[c], Amit Maity[d], Sixiang Shi[a,e*], Shreya Goel[a,e,f*]

[a] Department of Molecular Pharmaceutics, University of Utah, Salt Lake City, UT 84112, United States

[b] Department of Neurosurgery, Huntsman Cancer Institute, University of Utah, Salt Lake City, UT 84132, United States

[c] Department of Medical Physics, University of Wisconsin-Madison, Madison, WI 53705, United States

[d] Department of Radiation Oncology, School of Medicine, University of Utah, Salt Lake City, UT 84112, United States

[e] Department of Radiology and Imaging Sciences, University of Utah, Salt Lake City, UT 84112, United States

[f] Department of Biomedical Engineering, University of Utah, Salt Lake City, UT 84112, United States

*Correspondence to: sixiang.shi@utah.edu; shreya.goel@utah.edu

Abstract

Tumor hypoxia leads to increased resistance to radiation therapy (RT), resulting in markedly worse clinical outcomes in the treatment and management of pediatric malignant rhabdoid tumors (MRT). To alleviate hypoxia in MRT, we repurposed an FDA approved, mitochondrial oxidative phosphorylation (OXPHOS) inhibitor, Atovaquone (AVO), to inhibit oxygen consumption and thereby enhance the sensitivity of tumor cells to low dose RT in MRT by hypoxia alleviation. Additionally, to better understand the tumor response induced by AVO and optimize the combination with RT, we employed an emerging, noninvasive imaging modality, known as multispectral optoacoustic tomography (MSOT), to monitor and evaluate real-time dynamic changes in tumor hypoxia and vascular perfusion. Oxygen-Enhanced (OE)-MSOT could measure the change of tumor oxygenation in the MRT xenograft models after AVO and RT treatments, indicating its potential as a response biomarker. OE-MSOT showed that treating MRT mouse models with AVO resulted in a transient increase in oxygen saturation (ΔsO_2) in tumors when the mice were subjected to oxygen challenge, while RT or saline treated groups produced no change. In AVO+RT combination groups, the tumors showed an increase in ΔsO_2 after AVO administration followed by a significant decrease after RT, that correlated with a strong anti-tumor response, demarcated by complete regression of tumors, with no relapse on long-term monitoring. These observations were histologically validated. In MRT models of acquired AVO resistance, combination therapy failed to alleviate tumoral hypoxia and elicit any therapeutic benefit. Together, our data highlights the utility of repurposing anti-malarial AVO as an anticancer adjuvant for enabling low dose RT for pediatric patients.

INTRODUCTION

Malignant rhabdoid tumor (MRT) is a rare but one of the most lethal soft tissue cancers affecting infants and young children [1] with approximately 20 to 25 new cases diagnosed each year in the U.S. [2], and a median overall survival ranging from 6 to 17 months [3]. Three conventional treatments are commonly employed for MRT, varying in part based on the disease stage: surgery, X radiation therapy (RT) and chemotherapy [4]. Additionally, some new treatment modalities including immunotherapy [5, 6] and targeted therapy [7, 8] are also being tested in preclinical trials [9]. Nevertheless, considering most MRT patients are younger than three years old, there remains a need for continued consideration of the limitations associated with current treatments. For example, chemotherapy drugs sanctioned for treating MRT are often associated with heterogenous response and significant immediate and long-term toxicity in infant patients [10]. All patients are treated with high dose RT. However, RT is associated with late-stage side-effects such as growth and developmental delays in pediatric patients [11], as well as gastrointestinal dysfunction, pulmonary issues, infertility, cardiac abnormalities, and the potential for secondary cancers later in life [12]. Thus, to minimize immediate and long-term radiotoxicity, a safe and effective radiosensitizing adjuvant treatment to maximize RT efficiency at lower doses can become a “game-changer” in pediatric MRT management.

One of the features of the tumor microenvironment (TME) in nearly all solid tumors is diminished oxygen availability or tumor hypoxia [13], that results from increased oxygen consumption because of high metabolic demand and inefficient oxygen delivery due to leaky and compressed vessels [14]. Tumor hypoxia appears to be strongly associated with cancer progression, including epithelial-mesenchymal transition, tumor vascularization, angiogenesis, cell migration/invasion, metastasis, immunosuppression [15, 16], as well as poor outcomes for various treatment modalities including RT, as oxygen acts as a potent radiosensitizer, enhancing the DNA damage caused by ionizing radiation [17, 18]. Therefore, attenuation of hypoxia may be a highly appealing strategy to enhance the sensitivity of tumors to radiation and thereby improve therapeutic outcomes in pediatric MRT patients.

Currently, there are two common strategies employed to relieve tumor hypoxia: increasing oxygen delivery by exogenous oxygen supply or vascular remodeling, or, reducing demand for oxygen by modulating cellular oxygen consumption rate (OCR) through metabolic reprogramming [19-21]. Several signal transduction inhibitors for vascular remodeling, and physical strategies such as hyperbaric oxygen supply, oxygen-filled microbubbles etc to augment oxygen delivery, have been reported preclinically [22]. However, such strategies have failed to elicit reproducible responses in the clinic. Alternatively, minimizing mitochondrial oxygen consumption for reduction of OCR has emerged as a highly effective approach, with several mitochondrial inhibitors currently in various stages of preclinical and clinical investigation [23-28]. However, concerns regarding potential toxicity from high doses required, and suboptimal binding kinetics [29] have impacted their use as hypoxia modifiers. Atovaquone (AVO), as the first US Food and Drug Administration (FDA)-approved anti-malarial and anti-pneumocystis pneumonia drug, was recently repurposed as an antitumor drug by reducing OCR via suppressing mitochondrial oxidative phosphorylation (OXPHOS) that alleviates hypoxia in solid tumors [26]. AVO reduces OCR by inhibiting the mitochondrial electron transport chain at complex III, and studies have reported that AVO could effectively alleviate tumor hypoxia in various adult tumor types, as a monotherapy, as well as combination with radiotherapy and immunotherapy [30, 31]. However, to the best of our knowledge, such strategies have not been employed for pediatric tumors.

In this work, we investigate the application of AVO as a radiosensitizer in mouse models of pediatric MRT. To characterize the extent and duration of hypoxia modulation by AVO and to

optimize the outcomes of combination therapy, we employed multispectral optoacoustic tomography (MSOT), a multiscale imaging modality to noninvasively visualize oxygenation and vascular perfusion at the tumor site [32-34]. Data obtained at various wavelengths in optoacoustic tomography enables the computation of oxy- and deoxy-hemoglobin levels which can be employed to measure oxygen saturation (%sO_2) of the blood [35, 36]. By performing %sO_2 measurement following a switch of respiration gas from air (21% oxygen) to 100% oxygen, using the oxygen-enhanced (OE-MSOT) procedure, ΔsO_2 can be measured, that represents the "available oxygen capacity" in the tumor [37]. In addition to OE-MSOT, dynamic contrast enhanced (DCE)-MSOT can also be performed at the same time to evaluate tumor perfusion by analyzing NK^{trans} and K_{ep} pharmacokinetics (PK) parameters. These parameters respectively reflect the wash-in and wash-out perfusion rates of an FDA-approved agent, indocyanine green (ICG), within the tumor [38]. Thus, OE-MSOT and DCE-MSOT together can provide quantitative, multiparametric and extensive real-time functional information about tumor responses to administered AVO and RT in live animals.

Here, we integrated whole body optoacoustic imaging and statistical parametric mapping with tissue- and cellular scale histological analysis to predict and assess the effectiveness of AVO-potentiated low dose RT therapy in A-204 MRT xenografts **(Scheme 1)**. We found that at low pharmacologically achievable concentrations, AVO can effectively but transiently alleviate hypoxia in A-204 tumors, and strongly inhibit tumor growth in combination with a single 10 Gy X ray dose.

MATERIALS AND METHODS

Cell lines and Compounds

A-204 cell line was purchased from the American Type Culture Collection (ATCC). Cells were cultured at 37°C with 5% CO_2 in McCoy's 5A medium (ATCC) supplemented with 10% fetal bovine serum (FBS, GenClone) and 1% penicillin-streptomycin (GenClone). Atovaquone was obtained from Thermo Scientific. Bovine serum albumin (BSA) was obtained from Sigma. Matrigel was obtained from Huntsman Cancer Institute Preclinical Research Resource. Pimonidazole hydrochloride and Red 549 Mab were obtained from Hypoxyprobe™. Purified Rat Anti-mouse CD31 (Catalog No: 550274) was purchased from BD Biosciences. Alexa Fluor 488 AffiniPure Donkey Anti-Rat lgG(H+L) (Lot 163136) and Rhodamine (TRITC) AffiniPure Donkey Anti-Rat lgG(H+L) (Lot 157518) were obtained from Jackson ImmunoResearch Inc. Histone H2AX antibody (NB100-384) was purchased from Novus Biologicals and secondary antibody Donkey anti-Rabbit lgG (H+L) Dylight594 (SA5-10040) from Invitrogen. Purified anti-mouse/human Ki-67 antibody (151202) was purchased from Biolegend. The 2,5-diphenyltetrazolium bromide (MTT) assay (M6494) was obtained from ThermoFisher Scientific.

To model acquired resistance, atovaquone-resistant A-204 cell line (A^R-A-204) was established in house by gradient AVO treatment following slight modifications of previously published protocols [39].

Cell Viability Assay

To determine the cytotoxicity of AVO, MTT assay was carried out in A-204 and A^R-A-204 cells. The cells were seeded at a density of 2000 cells/well in a 96-well plate and cultured in McCoy's 5A culture medium at 37°C with 5% CO_2. After 24 hours incubation, cells in each well were treated with various concentrations of AVO (5, 10, 20, 50, 100, 200 and 500 µM) in 100 µL culture medium, with each concentration tested in 6 replicates. Following 72 hours of AVO treatment, MTT solution (10% 12 mM MTT stock solution) was added to each well and

incubated for 4 hours. The medium was then removed, and 50 μL of DMSO was added to each well. The cells were incubated for an additional 10 minutes at 37°C. The absorbance at 540 nm was determined using a microplate reader (Cytation 3, BioTek, USA) and the cell viability was calculated using the following equation:

$$\text{Cell Viability (\%)} = [\frac{\text{As} - \text{Ab}}{\text{Ac} - \text{Ab}}] \times 100$$

As = Absorbance of Test well;

Ab = Absorbance of Blank (medium only);

Ac = Absorbance of Control (cells only)

Seahorse Experiment

Real-time oxygen consumption rates (OCR) and extracellular acidification rates (ECAR) for A-204 and A^R-A-204 cells treated with AVO were determined using the XFPro Analyzer (Seahorse Biosciences). A-204 and A^R-A-204 cells were seeded in the Seahorse XF Pro cell culture microplate at a density of 20,000 cells/well and cultured at 37°C with 5% CO_2 in McCoy's 5A medium for 24 hours to allow attachment. Then, both A-204 and A^R-A-204 cells were treated with 25 μM AVO for 24 hours. Control groups treated with DMSO alone were processed in parallel. The measurements of the OCR were taken in XF assay medium containing 10 mM glucose. 1 mM pyruvate and 2 mM L-glutamine and 1 μM oligomycin, 0.5 μM phenyl-hydrazone (FCCP) and 0.5 μM rotenone/antimycin A were added sequentially for OCR measurement. ECAR measurements were taken in XF assay medium containing 1 mM pyruvate and 2 mM L-glutamine. 10 mM glucose, 2 μM oligomycin and 100 mM 2-DG were added for ECAR into the injection ports in the XF Pro sensor cartridge. 25 μM AVO was added into each well (excluding the DMSO wells) for the duration of the seahorse experiment. Measurements were normalized cell number, counted by adding 2 μM Hoechst 33342. OCR and ECAR data were analyzed with online seahorse analytics and Graphpad Prism 8.

Animal Models and Treatments

Mice were purchased from Charles River Laboratories. All animal experiments were conducted in accordance with the approved protocol by the Institutional Animal Care and Use Committee (IACUC) at the University of Utah. Wildtype A-204 (1×10^6) cells or AVO-resistant A^R-A-204 (1×10^6) cells (in PBS: Matrigel=1:1 solution) were inoculated subcutaneously in 26-44 days old athymic nude female mice. When the tumors reached around 50 mm^3, mice were randomized into treatment groups (n=5) that were given saline (control), AVO, RT (10 Gy) or the combination with AVO followed by RT. AVO was administered as an oral suspension of 50 mg kg^{-1} dose per day via oral gavage, following clinical dosing schedule [40]. Mice were given this dose for 7 days because AVO typically requires one or two weeks to achieve a consistent plasma concentration in human patients [41, 42]. Mice in RT or combination treatment cohorts received a single dose of 10 Gy X-ray irradiation focused on the tumor (CellRad, USA) on day 8, after 7 days of AVO treatment.

Mice were monitored for welfare throughout the study, and body weights were collected every day. Tumor size was measured with calipers and volume was calculated with the formula: [$V=(W^2 \times L)/2$]. Mice were euthanized (study endpoint) once the tumor reached 1000 mm^3, or if the body weight dropped 20% relative to baseline or if the mice were under poor bodily condition. After sacrifice, tumors and other organs were excised 1 hour after intraperitoneal (i.p.) administration of Pimonidazole hydrochloride (60 mg kg^{-1}). A^R-A-204 tumor-bearing mice were subjected to the same procedures.

In vivo MSOT Imaging

All *in vivo* MSOT imaging experiments were performed using iThera inVision 256-TF MSOT System (iThera Medical GmBH). OE-DCE MSOT were performed at day prior (referred to as Day-1 when the tumors reached to ~ 50 mm^3) for all treatment groups to establish baseline. Subsequently, for the saline and AVO-treated groups, longitudinal MSOT was conducted on Day 3, Day 9 and Day 23. For the 10 Gy and AVO+10 Gy-treated groups, MSOT scans were conducted on Day 3, Day 9, Day 16 and Day 30.

Briefly, A-204 or A^R-A-204 tumor-bearing mice were anesthetized using isoflurane and tail veins were catheterized. A thin layer of ultrasound gel (Aquasonic Clear, Parker Labs) was applied to facilitate optical and acoustic coupling with the polyethylene membrane. Subsequently, the mice were positioned in a lateral, side-lying orientation in a bag for imaging purposes. The chamber temperature was adjusted to 36 °C and the mice were allowed to equilibrate to the temperature for 10 minutes before imaging. This temperature allowed the mice to maintain 37 °C body temperature for the duration of the scan. Images were acquired at the largest tumor cross section of the mice with a step size of 1 mm. OE-DCE MSOT imaging was performed in the same scan session, following our previously published protocols [37]. For OE-MSOT scan, images were first acquired at 700 nm, 730 nm, 760 nm, 800 nm, 850 nm, and 875 nm wavelengths with 21% O_2 (air) breathing gas for 2 minutes. 10 frames and 20 repetitions were recorded at every imaging wavelength. The breathing gas was switched to 100% O_2. To allow the mice to reach equilibrium with 100% O_2, the mice remained in the chamber for 2 minutes without imaging. A second set of images were collected with 100% O_2 breathing gas for 2 minutes using the same parameters.

For DCE-MSOT scans, images were acquired at 700 nm, 730 nm, 760 nm, 800 nm, 850 nm, and 875 nm wavelengths under 100% O_2 breathing gas. 10 frames and 141 repetitions were recorded at every imaging wavelength. After 1 minute of acquiring pre-injection baseline images, indocyanine green (ICG, Sigma, 300 nmol, 100 µL) was intravenously injected and mice were scanned continuously for additional 15 minutes. ViewMSOT (Version_4.0), was utilized for image processing. Images were reconstructed using the Model Linear algorithm and fluence corrected (only for OE-MSOT scans) according to vendor presets. Spectral unmixing extracted the relative contribution of oxyhemoglobin (HbO_2) and deoxyhemoglobin (Hb), which were then utilized to produce blood oxygen saturation measurements ($\%sO_2^{air}$ and $\%sO_2^{O2}$) with each breathing gas. The difference between the average $\%sO_2^{air}$ and $\%sO_2^{O2}$ during their respective 2 minutes acquisitions was then used to determine ΔsO_2 within the tumor. For the DCE-MSOT scan, the pharmacokinetic rates of uptake (NK^{trans}) and wash-out (K_{ep}) of ICG were computed using our fluence-independent image analysis protocol [37, 43]. All parametric analyses for OE-DCE-MSOT scans was performed in MATLAB R2021b using our custom code (available upon request).

Histological Analysis

Tissues prepared for immunofluorescence were rinsed in PBS and preserved in OCT (Fisher HealthCare, USA) at -80°C. Tissues were cryo-sectioned into 5 µm thick sections (ARUP Laboratories, University of Utah) and stored at -80°C for further use. Prior to use, tissue sections were fixed with cold 4% PFA for 10 min and washed twice in PBS, followed by incubation in blocking buffer (5% BSA in PBS supplemented with 0.1 % Tween 20) for 1 hour. For pimonidazole staining, sections were stained with Red 549 dye-MAb (1:100, diluted in blocking buffer) overnight at 4°C and thoroughly washed twice in PBS. For CD31, γ-H2AX and Ki-67 staining, tissues were first incubated overnight at 4°C with primary rat anti-mouse CD31 (1:100, diluted in blocking buffer), primary rabbit γ-H2AX (1:100, diluted in blocking buffer) or primary rat anti-mouse/human Ki-67 (1:100, diluted in blocking buffer), respectively. After

washing twice with PBS, the sections were incubated for 1 hour at room temperature with secondary antibodies: Alexa Fluor 488 Affinipure Donkey Anti-Rat IgG (H+L) (1:200, diluted in blocking buffer), Dylight594 Donkey Anti-Rabbit IgG (H+L) (1:200, diluted in blocking buffer), or TRITC Affinipure Donkey Anti-Rat IgG (H+L) (1:200, diluted in blocking buffer) for CD31, γ-H2AX and Ki-67, respectively. Sections were washed twice in PBS, stained with 1 μg/mL DAPI for 10 minutes, followed by mounting buffer. All slides were stored at 4°C in a light-protected environment. Fluorescence images were acquired with the confocal laser scanning microscope (CLSM, Leica, SP8). At least 5 separate regions were imaged per tissue and 3 mice per group were analyzed for histological experiments. Whole tissue images were obtained on an Axioscan 7 slide scanner. For histological evaluation of tissues, 5 μm sections were obtained from the OCT cassettes and subsequently utilized for hematoxylin and eosin (H&E) staining. Slides were scanned at 40 × resolution using the Olympus biological microscope (Olympus BX41) and the images were processed using Amscope software.

Statistics

Statistical analysis was conducted using GraphPad Prism 8 software (GraphPad Software Inc.). The data were analyzed using Unpaired *t*-tests and One-Way ANOVA (multiple comparisons). Statistical significance between two groups was determined with two-tailed P-values: *P < 0.05, **P < 0.01, ***P < 0.001, and ****P < 0.0001. Survival was estimated by comparison of Kaplan-Meier curves using a log rank test.

RESULTS AND DISCUSSION

AVO effectively alleviates hypoxia by inhibiting mitochondrial function in A-204 cells

To verify the inhibitory effect of AVO on mitochondrial respiration, we measured the oxygen consumption rates (OCR) in A-204 cells using a Seahorse XF Pro analyzer. Control groups treated with DMSO alone were processed in parallel. Before measuring OCR traces, cytotoxicity experiments were conducted to determine the approximate AVO concentration for Seahorse experiments. As shown in **Figure 1A**, AVO monotherapy did not exert substantial cytotoxicity on A-204 cells, yielding an EC_{50} value ~28.36 μM. However, this concentration was sufficient to significantly suppress OXPHOS. Through the sequential injection of oligomycin, FCCP, rotenone/antimycin A, basal respiration, maximal respiration and ATP production of A-204 cells were recorded. OCR traces shown in **Figure 1B-E** demonstrated that AVO-treated groups exhibited significant suppression in basal respiration, maximal respiration and ATP production compared with the control groups, indicating AVO can effectively inhibit mitochondrial respiration.

We also compared the performance of AVO with Metformin, another most commonly applied OXPHOS inhibitor. As seen in **Figure S1**, the EC_{50} value of Metformin for A-204 cells was found to be 13.15 mM, which was significantly higher than that of AVO (~28.36 μM). This confirms that AVO could potentially lead to better therapeutic effects and less toxicity at lower concentrations, suggesting improved *in vivo* performance when compared to metformin.

In vivo OE-MSOT imaging shows that AVO treatment improves tumor oxygenation transiently

We investigated the *in vivo* pharmacodynamics of AVO treatment on A-204 xenografts using longitudinal OE-MSOT. OE-MSOT maps tumor oxygenation based on changes in hemoglobin oxygen saturation (%SO_2, computed as a ratio of HbO_2 to total Hemoglobin) following the delivery of supplemental (100%) oxygen. ΔsO_2 parameter is computed as the difference between $\%sO_2^{O2}$ and $\%sO_2^{air}$. Compared to static MSOT measurements, dynamic nature of OE-

MSOT has been found to provide more robust and reproducible spatiotemporal evaluations of tumor oxygenation [44-46]. We hypothesized that hypoxic tumors will be refractory to hyperoxic gas breathing as high oxygen consumption will increase oxygen extraction rate, resulting in a reduction of hemoglobin bound O_2 (HbO_2). Meanwhile, reduction in metabolic oxygen consumption by AVO will require reduction in oxygen extraction, resulting in greater affinity of oxygen for hemoglobin, and hence higher $\%sO_2^{O2}$ after hyperoxic gas challenge.

Application of oxygen gas challenge on tumors at baseline (referred to as day-1, when tumors reached ~ 50 mm^3) indicated negligible changes in the MSOT derived $\%sO_2$ when switching from air to 100% oxygen, indicating the hypoxic nature of the tumors (**Figure S2**). **Figure 2B** and **C** show that AVO treated tumors depicted a nearly 2-fold increase in ΔsO_2 from baseline (ΔsO_2 = 0.047 ± 0.02) at day 3 (ΔsO_2 = 0.094 ± 0.05) when compared to saline treated controls (ΔsO_2 = 0.050 ± 0.002 at day -1 and 0.030 ± 0.011 at day 3). After AVO treatment was stopped at day 7, the tumors gradually revert to a hypoxic phenotype. The tumors remained well-oxygenated on day 9 compared to saline treated controls (p=0.0074). OE-MSOT at endpoint (day 23 for AVO treated group) showed a strong reduction in ΔsO_2 (0.011 ± 0.007) which is comparable to saline-treated controls at endpoint (day 30; 0.016 ± 0.011). This decrease in ΔsO_2 can be attributed an increase in tumor volume. Increase pimonidazole immunofluorescence (**Figure 3A, 3B** and **Figure S3**) validated our *in vivo* OE-MSOT observations.

As the duration of hypoxia alleviation by AVO is short-lived and wanes off soon after treatment is stopped, it is imperative that combination with radiotherapy is timed appropriately, such that the tumors are irradiated when they are most oxygenated. Our results highlight the importance of longitudinal monitoring of hypoxia modulation by AVO using OE-MSOT. After establishing the oxygenation dynamics, a separate cohort of AVO-treated tumor-bearing mice were subjected to a single low 10 Gy dose of focused X-radiation, one day after AVO treatment was stopped. *Ex vivo* pimonidazole staining confirmed the well-oxygenated status of tumors at day 8 (**Figure 3A** and **Figure 3D(a)**) Immediate (day 9) and longer-term changes in tumor oxygenation following AVO+10 Gy combination treatment was assessed with OE-MSOT and immunofluorescence and compared to mice receiving 10 Gy irradiation only. As seen in **Figure 2E** and **F**, irradiation of AVO-treated tumors results in an immediate and strong decrease in ΔsO_2 (0.044 ± 0.002) at day 9 compared to ΔsO_2 (0.142 ± 0.021) at day 3 (p value =0.0013), presumably caused by enhanced cellular death. We hypothesized that increased oxygenation by AVO bolstered greater ROS-mediated cell killing by low dose radiation. Interestingly, we observed a slight increase in tumor oxygenation a few days after irradiation, as measured by both OE-MSOT and pimonidazole immunostaining (**Figure 3B, 3D(b)** and **Figure S3**). It is reasonable to assume that increased cellular apoptosis resulted in reduced oxygen consumption and hence a temporary increase in intratumoral oxygen levels. Ki-67 staining and H&E on day 12 validated our premise (**Figure 3C**and **Figure 3D(c)**). To confirm that hypoxia modulation by AVO was tumor specific, and to confirm that pimonidazole staining truly reflected tissue oxygenation, we assessed major organs (heart, liver, kidney and muscle) in saline and AVO+10 Gy treated groups. As seen in **Figure S4**, no significant difference was observed in pimonidazole staining for any of the tissues between saline and AVO+10 Gy groups.

In contrast, tumors treated with irradiation only remained uniformly hypoxic with no significant changes in ΔsO_2 values, consistent with resistance to low dose radiotherapy (**Figure 2E** and **Figure 2F**). Pimonidazole staining of irradiated tumors on day 9 and endpoint indicated similar hypoxia levels as saline treated groups, which further corroborated our observations *in vivo*. Taken together, our data indicates the potential utility of monitoring oxygenation by OE-MSOT and ΔsO_2 as a noninvasive biomarker to predict and evaluate tumor response to hypoxia modulating therapies and radiotherapy. As MSOT involves light and ultrasound for noninvasive

interrogation of tissues, we believe it could be an attractive modality for imaging-based treatment planning and evaluation in children with cancers.

AVO enhances the sensitivity of A-204 tumors to low dose radiation therapy

Given the significant improvement in tumor oxygenation after AVO treatment observed by OE-MSOT and pimonidazole staining, we hypothesized that AVO could enhance the sensitivity of A-204 tumors to low dose radiation therapy and improve tumor responses. Thus, after imaging, mice in monotherapy and combination therapy groups were monitored for tumor growth and survival over 60 days (**Figure 4A**). Mouse body weight was also measured, as weight changes serve as a valuable parameter for assessing treatment toxicity *in vivo* [47]. As shown in **Figure 4B**, the body weight curves exhibited no significant difference among all treatment groups, suggesting that AVO, 10 Gy or combined treatments did not cause noticeable systemic toxic effects on mice, compared to saline treated controls. Tumor volume changes (**Figure 4C**) showed that the average time required for tumors to reach 1000 mm^3 was 29 days for saline-treated group, 30 days for AVO-treated group and 42 days for 10 Gy-treated group. One tumor in the RT only group had excellent response. However, for the AVO+10 Gy-treated group, all the tumors were completely abolished within 10 days post-treatment, and most strikingly, tumors did not recur for the remainder of the study. Endpoint tumor volume changes as measured by calipers (**Figure 4D**) or observed visually (**Figure S5** and **Figure 4E**) demonstrated significant abrogation of tumors in all mice treated with AVO+10 Gy when compared to monotherapy or saline treated mice (p value <0.0001). As expected, the stellar tumor inhibitory effects of AVO + RT combination therapy, coupled with minimal toxicity resulted in significantly extended animal survival (**Figure 4F**).

We used γ-H2AX as a biomarker of DNA damage to evaluate irradiation response in A-204 tumors [48]. As seen in **Figure 5A** and **B,** AVO+10 Gy-treated tumors depicted more obvious γ-H2AX signal when compared to saline-treated (p=0.0038), AVO-treated (p=0.0011) and 10 Gy-treated groups (p=0.0284; **Figure 5C(b)**), demonstrating the radiosensitizing effect of AVO on typically radioresistant tumors. Subsequently, H&E staining of other organs including heart, liver, kidney and muscle was performed to further evaluate the treatment toxicity. As shown in **Figure 5D**, no detectable necrosis or morphological changes were observed in these organs, which is consistent with the conclusions drawn from the body weight results.

To test whether increased radiation doses would elicit tumor inhibitory effects, a separate cohort of A-204 xenografted mice were treated with 30 Gy dose (fractionated over 5 days, 6 Gy per fraction). Another group of mice was treated with AVO and fractionated RT dose (treatment schema shown in **Figure S6**). As seen in **Figure S6A**, a fractionated 30 Gy dose was well-tolerated (no apparent change in body weight) but only succeeded in slowing the tumor growth. In one mouse, the tumor did not respond to irradiation, as indicated by the exponential increase in tumor volume. On the hand, when combined with AVO, a 30 Gy fractionated dose exerted significant tumor control, with tumors disappearing within 5 days of stopping treatment (**Figure S6B**).

Taken together, the data demonstrate that the combination of AVO and radiation therapy is an effective and efficient strategy to maximize responses, with potential for clinical application in MRT treatment in the future. Our findings are significant for children with MRT through two avenues. First, we demonstrate that AVO can serve as a safe, FDA approved adjuvant to significantly enhance therapeutic efficacy of radiotherapy in otherwise radioresistant tumors, improving overall recurrence-free survival. Second, the ability to obliterate tumors at low radiation doses serves to greatly assuage concerns about longer-term radiotoxicities or secondary tumor growth, which are known to significantly impact quality of life and survival in patients subjected to aggressive chemoradiation therapies, earlier in childhood.

Atovaquone-resistant A-204 xenografts are no longer sensitive to radiotherapy

To confirm that AVO was indeed essential for the observed therapeutic efficacy of RT, we developed AVO-resistant A-204 cell line (A^R-A-204) by treating cells to escalating doses of AVO over time (**Figure 6A**). OCR and ECAR traces were first assessed in A^R-A-204 cells after treating with 25 µM AVO for 24 hours. The results shown in **Figure 6B** indicated that continuous AVO treatment inhibited mitochondrial respiration in A^R-A-204 cells, significantly reducing basal respiration, maximal respiration, and ATP production (p value <0.0001, **Figure 6D-F**). Conversely, ECAR results showed a significant increase in aerobic glycolysis in A^R-A-204 cells (**Figure 6C**), with marked improvements in glycolytic reserve (p value =0.0002) and glycolytic reserve capacity (p value <0.0001, **Figure S7**). This suggested that continuous AVO treatment shifted A-204 cells from an oxidative state to a glycolytic state.

Next, A^R-A-204 xenografts were treated with saline or AVO+10 Gy combination and tumor oxygenation was monitored longitudinally using OE-MSOT. As seen in **Figures 6G** and **H**, saline-treated A^R-A-204 tumor exhibited higher oxygenation levels at all time points (ΔsO_2 = 0.048 ± 0.01 at day 3; ΔsO_2 = 0.035 ± 0.01 at day 9 and ΔsO_2 = 0.027 ± 0.003 at day 23) when compared to saline-treated A-204 tumors (**Figure 2C**; ΔsO_2 = 0.030 ± 0.011 at day 3, ΔsO_2 = 0.030 ± 0.007 at day 9 and ΔsO_2 = 0.016 ± 0.01 at day 23). This finding suggests that constitutive inhibition of OXPHOS in A^R-A-204, results in less severe hypoxic TME in MRT, despite a shift towards glycolytic metabolism. Lower pimonidazole immunofluorescence signals (**Figure 6I** and **Figure 6J**) validated our *in vivo* OE-MSOT observations. Further, in the AVO+10 Gy-treated A^R-A-204 xenografts **(Figures 6G** and **Figure 6H)**, OE-MSOT at midpoint revealed no difference from saline treated groups and a significant decrease in ΔsO_2 (day 3; 0.042 ± 0.01), contrasting with the A-204 xenografts (**Figure 2E**; day 3; 0.142 ± 0.02), which confirms that A^R-A-204 xenografts no longer respond to AVO treatment and hypoxia alleviation seen in wildtype A-204 tumors was solely reliant on AVO-mediated OXPHOS inhibition. Pimonidazole exhibited an obvious higher signal in the AVO+10 Gy group (**Figure 6I**) compared to the wildtype A-204 combination treatment group, further supporting our OE-MSOT observations.

Since AVO treatment did not alleviate hypoxia in the A^R-A-204 xenografts, we further investigated and validated whether the treatment response of AVO+10 Gy would also be diminished in these tumors. As shown in **Figure 7A**, there was no significant fluctuation in body weight, except for one mouse in the AVO+10 Gy-treated group, which experienced around 25% weight reduction relative to baseline immediately after receiving 10 Gy irradiation. Therefore, this mouse has been excluded for the subsequent study. The survival rates and tumor volume changes (**Figure 7B** and **Figure 7C**) showed that the average time required for tumors to reach 1000 mm^3 was 40 days for the saline-treated group. The tumor growth was significantly slower compared to the 29 days (to reach endpoint) observed in saline treated wildtype A-204 tumors, suggesting that the OXPHOS abrogation and shift towards a glycolytic phenotype could make MRT less aggressive. Mice treated with AVO + 10Gy combination treatment, took an average of 54 days to reach 1000 mm^3. Although the tumor volume showed a slight reduction after the treatment on day 9, the tumor continued to grow in the following weeks, indicating A^R-A-204 tumors did not benefit from the therapy (**Figure 7C and Figure 7D**), suggesting that AVO no longer exerted a radiosensitizing effect in resistant xenografts. As shown in **Figure 7E**, H&E staining showed no significant toxicity observed in the normal organs including heart, liver, kidney and muscle and no detectable morphological changes or apparent necrosis was observed in the tumors excised from either saline or combination therapy cohorts.

DCE-MSOT indicates that AVO-mediated reduction in tumor hypoxia does not depend on vascular normalization

Prolonged hypoxia could result from irregular tumor vascularization in aggressive solid tumors [49], which compromises tumor perfusion and hinders effective oxygen delivery [50].To establish whether AVO treatment could relieve tumoral hypoxia by vascular normalization, we employed DCE-MSOT to visualize and quantify changes in tumor vascular perfusion. **Figure 8A** displays the parametric maps of normalized wash-in rate (NK^{trans}) and wash-out rate (K_{ep}) of ICG for the saline and AVO-treated groups on Day-1 (baseline), and Days 3, 9 and 23. There were no significant differences detected in NK^{trans} and K_{ep} values before, during, and after AVO treatment (**Figure 8B**). Kinetic curves plotted for ICG accumulation over 15 minutes of dynamic scan demonstrated no apparent differences between tumors treated with saline or AVO (**Figure 8C**). These results, together with our *in vivo* OE-MSOT and *ex vivo* histopathological data establish that improved tumor oxygenation by AVO is mediated by associated reduction in metabolic demand for oxygen and not through vascular normalization. Furthermore, we also compared the parametric maps, NK^{trans} and K_{ep} values, and ICG signal kinetics in the tumors of 10 Gy monotherapy and AVO+10 Gy combination treatment groups. The results of **Figure S8A** and **B** indicate that no meaningful difference was observed between the different groups. Interestingly, although changes in vascular perfusion are commonly observed after RT in solid tumors, we did not find any significant alterations in our study, possibly attributed to the intrinsic radioresistance of MRT to low dose radiation.

Immunofluorescence imaging of CD31 was subsequently conducted on excised tumor tissues at day 9 (**Figure S8C**) and endpoint **(Figure S9)** to validate our *in vivo* findings. Consistent with the DCE-MSOT results, CD31 staining did not show any significant difference among different treatment groups, suggesting that AVO had no impact on vessel functionality.

CONCLUSIONS

In this study, we developed a clinically translatable combination strategy to enhance the radiation response of pediatric rhabdoid tumors to low X ray doses by repurposing a mitochondrial inhibitor AVO as a hypoxia modifier. Our results revealed that short term (7 day) AVO treatment at pharmacologically viable doses could effectively improve the oxygenation levels in A-204 tumors, and thereby result in long-term inhibition of tumor growth when combined with a single 10 Gy X ray dose. Furthermore, the real-time changes of oxygenation could be visualized and monitored before, during, and after the treatment by implementing photoacoustic imaging, a safe, widely available, and noninvasive imaging modality. As it is free from ionizing radiation, we posit that MSOT can be easily and safely implemented to guide and optimize treatment schedules and evaluate treatment response to AVO-enhanced RT in pediatric MRT patients.

There are several advantages to our treatment and imaging strategy. Given that most patients with rhabdoid tumors are under 3 years old, using an orally bioavailable, FDA approved, off-label drug, AVO to radiosensitize MRT in the clinic can be easily and quickly envisaged, as opposed to other radiosensitizers currently under development that would need to undergo IND approval. Our data establishes that AVO reduces the effective radiation dose required to achieve the maximum therapeutic effect, which makes radiation therapy safer for pediatric patients both in the long and short term. Furthermore, by measuring changes in tumor oxygenation in a label-free, noninvasive manner, we can receive immediate and repeated feedback whether AVO-enhanced RT works in a patient, allowing for real-time, personalized treatment adjustment. Frequent monitoring enabled by an ionizing radiation-free imaging modality would spare the pediatric patients from ineffective or toxic over-treatment. Although clinical trials with AVO are currently underway in adult cancers, the results of our study provide a

strong foundation for advancing the drug to benefit children with MRT and other radioresistant cancers.

Acknowledgements

This work was supported, in part, by the University of Utah, the University of Utah Immunology, Inflammation and Infectious Diseases (3i) Initiative, the 5 For the Fight Fellowship, and the Elsa U Pardee Foundation. We acknowledge support from the University of Utah school of Medicine and Vice President for Research seed grant and Research Instrumentation Fund. We acknowledge direct financial support by the National Cancer Institute of the National Institutes of Health under Award Number P30CA042014.

Disclosures

The authors declare no competing interests.

References

[1] A. Biswas, L. Kashyap, A. Kakkar, C. Sarkar, P.K. Julka, Atypical teratoid/rhabdoid tumors: challenges and search for solutions, Cancer Management and Research, 8 (2016) 115-125.
[2] S.K. Wang, P. Mannam, K. Dukleska, F. Balarezo, Congenital Disseminated Malignant Rhabdoid Tumor Mimicking a Vascular Lesion, Cureus, 16 (2024) e58337.
[3] D.L. Buscariollo, H.S. Park, K.B. Roberts, J.B. Yu, Survival outcomes in atypical teratoid rhabdoid tumor for patients undergoing radiotherapy in a Surveillance, Epidemiology, and End Results analysis, Cancer, 118 (2012) 4212-4219.
[4] K. Nemes, P.D. Johann, S. Tüchert, P. Melchior, C. Vokuhl, R. Siebert, R. Furtwängler, M.C. Frühwald, Current and Emerging Therapeutic Approaches for Extracranial Malignant Rhabdoid Tumors, Cancer Management and Research, 14 (2022) 479-498.
[5] R.G. Majzner, J.L. Theruvath, A. Nellan, S. Heitzeneder, Y. Cui, C.W. Mount, S.P. Rietberg, M.H. Linde, P. Xu, C. Rota, E. Sotillo, L. Labanieh, D.W. Lee, R.J. Orentas, D.S. Dimitrov, Z. Zhu, B.S. Croix, A. Delaidelli, A. Sekunova, E. Bonvini, S.S. Mitra, M.M. Quezado, R. Majeti, M. Monje, P.H.B. Sorensen, J.M. Maris, C.L. Mackall, CAR T Cells Targeting B7-H3, a Pan-Cancer Antigen, Demonstrate Potent Preclinical Activity Against Pediatric Solid Tumors and Brain Tumors, Clin Cancer Res, 25 (2019) 2560-2574.
[6] J. Theruvath, E. Sotillo, C.W. Mount, C.M. Graef, A. Delaidelli, S. Heitzeneder, L. Labanieh, S. Dhingra, A. Leruste, R.G. Majzner, P. Xu, S. Mueller, D.W. Yecies, M.A. Finetti, D. Williamson, P.D. Johann, M. Kool, S. Pfister, M. Hasselblatt, M.C. Frühwald, O. Delattre, D. Surdez, F. Bourdeaut, S. Puget, S. Zaidi, S.S. Mitra, S. Cheshier, P.H. Sorensen, M. Monje, C.L. Mackall, Locoregionally administered B7-H3-targeted CAR T cells for treatment of atypical teratoid/rhabdoid tumors, Nat Med, 26 (2020) 712-719.
[7] J. Torchia, B. Golbourn, S. Feng, K.C. Ho, P. Sin-Chan, A. Vasiljevic, J.D. Norman, P. Guilhamon, L. Garzia, N.R. Agamez, M. Lu, T.S. Chan, D. Picard, P. de Antonellis, D.A. Khuong-Quang, A.C. Planello, C. Zeller, D. Barsyte-Lovejoy, L. Lafay-Cousin, L. Letourneau, M. Bourgey, M. Yu, D.M.A. Gendoo, M. Dzamba, M. Barszczyk, T. Medina, A.N. Riemenschneider, A.S. Morrissy, Y.S. Ra, V. Ramaswamy, M. Remke, C.P. Dunham, S. Yip, H.K. Ng, J.Q. Lu, V. Mehta, S. Albrecht, J. Pimentel, J.A. Chan, G.R. Somers, C.C. Faria, L. Roque, M. Fouladi, L.M. Hoffman, A.S. Moore, Y. Wang, S.A. Choi, J.R. Hansford, D. Catchpoole, D.K. Birks, N.K. Foreman, D. Strother, A. Klekner, L. Bognár, M. Garami, P. Hauser, T. Hortobágyi, B. Wilson, J. Hukin, A.S. Carret, T.E. Van Meter, E.I. Hwang, A. Gajjar, S.H. Chiou, H. Nakamura, H. Toledano, I. Fried, D. Fults, T. Wataya, C. Fryer, D.D. Eisenstat, K. Scheinemann, A.J. Fleming, D.L. Johnston, J. Michaud, S. Zelcer, R. Hammond, S. Afzal, D.A. Ramsay, N. Sirachainan, S. Hongeng, N. Larbcharoensub, R.G. Grundy, R.R. Lulla, J.R. Fangusaro, H. Druker, U. Bartels, R. Grant, D. Malkin, C.J. McGlade, T. Nicolaides, T. Tihan, J. Phillips, J. Majewski, A. Montpetit,

G. Bourque, G.D. Bader, A.T. Reddy, G.Y. Gillespie, M. Warmuth-Metz, S. Rutkowski, U. Tabori, M. Lupien, M. Brudno, U. Schüller, T. Pietsch, A.R. Judkins, C.E. Hawkins, E. Bouffet, S.K. Kim, P.B. Dirks, M.D. Taylor, A. Erdreich-Epstein, C.H. Arrowsmith, D.D. De Carvalho, J.T. Rutka, N. Jabado, A. Huang, Integrated (epi)-Genomic Analyses Identify Subgroup-Specific Therapeutic Targets in CNS Rhabdoid Tumors, Cancer Cell, 30 (2016) 891-908.
[8] J.M. Maris, C.L. Morton, R. Gorlick, E.A. Kolb, R. Lock, H. Carol, S.T. Keir, C.P. Reynolds, M.H. Kang, J. Wu, M.A. Smith, P.J. Houghton, Initial testing of the aurora kinase A inhibitor MLN8237 by the Pediatric Preclinical Testing Program (PPTP), Pediatr Blood Cancer, 55 (2010) 26-34.
[9] M.F. Weingart, J.J. Roth, M. Hutt-Cabezas, T.M. Busse, H. Kaur, A. Price, R. Maynard, J. Rubens, I. Taylor, X.G. Mao, J. Xu, Y. Kuwahara, S.J. Allen, A. Erdreich-Epstein, B.E. Weissman, B.A. Orr, C.G. Eberhart, J.A. Biegel, E.H. Raabe, Disrupting LIN28 in atypical teratoid rhabdoid tumors reveals the importance of the mitogen activated protein kinase pathway as a therapeutic target, Oncotarget, 6 (2015) 3165-3177.
[10] A.D. Trobaugh-Lotrario, M.J. Finegold, J.H. Feusner, Rhabdoid tumors of the liver: Rare, aggressive, and poorly responsive to standard cytotoxic chemotherapy, Pediatric Blood & Cancer, 57 (2011) 423-428.
[11] D.A. Rodeberg, M.D. Wharam, E.R. Lyden, J.A. Stoner, K. Brown, S.L. Wolden, C.N. Paidas, S.S. Donaldson, D.S. Hawkins, S.L. Spunt, C.A. Arndt, Delayed primary excision with subsequent modification of radiotherapy dose for intermediate-risk rhabdomyosarcoma: a report from the Children's Oncology Group Soft Tissue Sarcoma Committee, International journal of cancer, 137 (2015) 204-211.
[12] V. Jairam, K.B. Roberts, J.B. Yu, Historical trends in the use of radiation therapy for pediatric cancers: 1973-2008, International journal of radiation oncology, biology, physics, 85 (2013) e151-155.
[13] A. Rakotomalala, A. Escande, A. Furlan, S. Meignan, E.J.F.i.e. Lartigau, Hypoxia in solid tumors: how low oxygenation impacts the “Six Rs” of radiotherapy, 12 (2021) 742215.
[14] H. Scholz, F.J. Boivin, K.M. Schmidt-Ott, S. Bachmann, K.-U. Eckardt, U.I. Scholl, P.B.J.N.R.N. Persson, Kidney physiology and susceptibility to acute kidney injury: implications for renoprotection, 17 (2021) 335-349.
[15] C.M. Neophytou, M. Panagi, T. Stylianopoulos, P.J.C. Papageorgis, The role of tumor microenvironment in cancer metastasis: Molecular mechanisms and therapeutic opportunities, 13 (2021) 2053.
[16] A. Sebestyén, L. Kopper, T. Dankó, J.J.P. Tímár, O. Research, Hypoxia signaling in cancer: from basics to clinical practice, 27 (2021) 1609802.
[17] W. Bouleftour, E. Rowinski, S. Louati, S. Sotton, A.S. Wozny, P. Moreno-Acosta, B. Mery, C. Rodriguez-Lafrasse, N. Magne, A Review of the Role of Hypoxia in Radioresistance in Cancer Therapy, Med Sci Monit, 27 (2021) e934116.
[18] C. Peitzsch, R. Perrin, R.P. Hill, A. Dubrovska, I. Kurth, Hypoxia as a biomarker for radioresistant cancer stem cells, International Journal of Radiation Biology, 90 (2014) 636-652.
[19] P. Marchetti, Q. Fovez, N. Germain, R. Khamari, J. Kluza, Mitochondrial spare respiratory capacity: Mechanisms, regulation, and significance in non-transformed and cancer cells, The FASEB Journal, 34 (2020) 13106-13124.
[20] R.H. Farnsworth, M. Lackmann, M.G. Achen, S.A. Stacker, Vascular remodeling in cancer, Oncogene, 33 (2014) 3496-3505.
[21] K. Matuszewska, M. Pereira, D. Petrik, J. Lawler, J. Petrik, Normalizing Tumor Vasculature to Reduce Hypoxia, Enhance Perfusion, and Optimize Therapy Uptake, Cancers (Basel), 13 (2021).
[22] J.R. Eisenbrey, L. Albala, M.R. Kramer, N. Daroshefski, D. Brown, J.-B. Liu, M. Stanczak, P. O’Kane, F. Forsberg, M.A. Wheatley, Development of an ultrasound sensitive oxygen carrier for oxygen delivery to hypoxic tissue, International Journal of Pharmaceutics, 478 (2015) 361-367.

[23] X. Zhou, J. Chen, G. Yi, M. Deng, H. Liu, M. Liang, B. Shi, X. Fu, Y. Chen, L. Chen, Z. He, J. Wang, J. Liu, Metformin suppresses hypoxia-induced stabilization of HIF-1α through reprogramming of oxygen metabolism in hepatocellular carcinoma, Oncotarget, 7 (2016) 873-884.
[24] A. Tsuji, T. Akao, T. Masuya, M. Murai, H. Miyoshi, IACS-010759, a potent inhibitor of glycolysis-deficient hypoxic tumor cells, inhibits mitochondrial respiratory complex I through a unique mechanism, Journal of Biological Chemistry, 295 (2020) 7481-7491.
[25] M. Benej, X. Hong, S. Vibhute, S. Scott, J. Wu, E. Graves, Q.T. Le, A.C. Koong, A.J. Giaccia, B. Yu, C.S. Chen, I. Papandreou, N.C. Denko, Papaverine and its derivatives radiosensitize solid tumors by inhibiting mitochondrial metabolism, Proc Natl Acad Sci U S A, 115 (2018) 10756-10761.
[26] M. Skwarski, D.R. McGowan, E. Belcher, F. Di Chiara, D. Stavroulias, M. McCole, J.L. Derham, K.Y. Chu, E. Teoh, J. Chauhan, D. O'Reilly, B.H.L. Harris, P.S. Macklin, J.A. Bull, M. Green, G. Rodriguez-Berriguete, R. Prevo, L.K. Folkes, L. Campo, P. Ferencz, P.L. Croal, H. Flight, C. Qi, J. Holmes, J.P.B. O'Connor, F.V. Gleeson, W.G. McKenna, A.L. Harris, D. Bulte, F.M. Buffa, R.E. Macpherson, G.S. Higgins, Mitochondrial Inhibitor Atovaquone Increases Tumor Oxygenation and Inhibits Hypoxic Gene Expression in Patients with Non-Small Cell Lung Cancer, Clin Cancer Res, 27 (2021) 2459-2469.
[27] F. Janku, P. LoRusso, A.S. Mansfield, R. Nanda, A. Spira, T. Wang, A. Melhem-Bertrandt, J. Sugg, H.A. Ball, First-in-human evaluation of the novel mitochondrial complex I inhibitor ASP4132 for treatment of cancer, Invest New Drugs, 39 (2021) 1348-1356.
[28] T.A. Yap, N. Daver, M. Mahendra, J. Zhang, C. Kamiya-Matsuoka, F. Meric-Bernstam, H.M. Kantarjian, F. Ravandi, M.E. Collins, M.E.D. Francesco, E.E. Dumbrava, S. Fu, S. Gao, J.P. Gay, S. Gera, J. Han, D.S. Hong, E.J. Jabbour, Z. Ju, D.D. Karp, A. Lodi, J.R. Molina, N. Baran, A. Naing, M. Ohanian, S. Pant, N. Pemmaraju, P. Bose, S.A. Piha-Paul, J. Rodon, C. Salguero, K. Sasaki, A.K. Singh, V. Subbiah, A.M. Tsimberidou, Q.A. Xu, M. Yilmaz, Q. Zhang, Y. Li, C.A. Bristow, M.B. Bhattacharjee, S. Tiziani, T.P. Heffernan, C.P. Vellano, P. Jones, C.J. Heijnen, A. Kavelaars, J.R. Marszalek, M. Konopleva, Complex I inhibitor of oxidative phosphorylation in advanced solid tumors and acute myeloid leukemia: phase I trials, Nat Med, 29 (2023) 115-126.
[29] M. Ikeda, A. Sato, N. Mochizuki, K. Toyosaki, C. Miyoshi, R. Fujioka, S. Mitsunaga, I. Ohno, Y. Hashimoto, H. Takahashi, H. Hasegawa, S. Nomura, R. Takahashi, S. Yomoda, K. Tsuchihara, S. Kishino, H. Esumi, Phase I trial of GBS-01 for advanced pancreatic cancer refractory to gemcitabine, Cancer Sci, 107 (2016) 1818-1824.
[30] M. Fiorillo, R. Lamb, H.B. Tanowitz, L. Mutti, M. Krstic-Demonacos, A.R. Cappello, U.E. Martinez-Outschoorn, F. Sotgia, M.P. Lisanti, Repurposing atovaquone: targeting mitochondrial complex III and OXPHOS to eradicate cancer stem cells, Oncotarget, 7 (2016) 34084-34099.
[31] T.M. Ashton, E. Fokas, L.A. Kunz-Schughart, L.K. Folkes, S. Anbalagan, M. Huether, C.J. Kelly, G. Pirovano, F.M. Buffa, E.M. Hammond, M. Stratford, R.J. Muschel, G.S. Higgins, W.G. McKenna, The anti-malarial atovaquone increases radiosensitivity by alleviating tumour hypoxia, Nat Commun, 7 (2016) 12308.
[32] S. Dey, S. Kumari, S.P. Kalainayakan, J. Campbell, 3rd, P. Ghosh, H. Zhou, K.E. FitzGerald, M. Li, R.P. Mason, L. Zhang, L. Liu, The vascular disrupting agent combretastatin A-4 phosphate causes prolonged elevation of proteins involved in heme flux and function in resistant tumor cells, Oncotarget, 9 (2018) 4090-4101.
[33] L.J. Rich, M. Seshadri, Photoacoustic imaging of vascular hemodynamics: validation with blood oxygenation level-dependent MR imaging, Radiology, 275 (2015) 110-118.
[34] I. Quiros-Gonzalez, M.R. Tomaszewski, S.J. Aitken, L. Ansel-Bollepalli, L.A. McDuffus, M. Gill, L. Hacker, J. Brunker, S.E. Bohndiek, Optoacoustics delineates murine breast cancer models displaying angiogenesis and vascular mimicry, Br J Cancer, 118 (2018) 1098-1106.
[35] E. Brown, J. Brunker, S.E. Bohndiek, Photoacoustic imaging as a tool to probe the tumour microenvironment, Disease models & mechanisms, 12 (2019).

[36] G. Balasundaram, L. Ding, X. Li, A.B.E. Attia, X.L. Dean-Ben, C.J.H. Ho, P. Chandrasekharan, H.C. Tay, H.Q. Lim, C.B.J.T.o. Ong, Noninvasive anatomical and functional imaging of orthotopic glioblastoma development and therapy using multispectral optoacoustic tomography, 11 (2018) 1251-1258.
[37] G. Shreya, C. Jorge de la, S. William, K. Aikaterini, C.-R. Julio, P. Mark, Evaluations of radiotherapy in small animal models of pancreatic cancer with oxygen enhanced–dynamic contrast enhanced multispectral optoacoustic tomography (OE-DCE MSOT), Proc.SPIE, 2023, pp. 123791B.
[38] J.A. Carr, D. Franke, J.R. Caram, C.F. Perkinson, M. Saif, V. Askoxylakis, M. Datta, D. Fukumura, R.K. Jain, M.G. Bawendi, O.T. Bruns, Shortwave infrared fluorescence imaging with the clinically approved near-infrared dye indocyanine green, Proceedings of the National Academy of Sciences, 115 (2018) 4465-4470.
[39] L. Au - Mohr, M. Au - Carceles-Cordon, J. Au - Woo, C. Au - Cordon-Cardo, J. Au - Domingo-Domenech, V. Au - Rodriguez-Bravo, Generation of Prostate Cancer Cell Models of Resistance to the Anti-mitotic Agent Docetaxel, JoVE, (2017) e56327.
[40] J. Falloon, S. Sargent, S.C. Piscitelli, C. Bechtel, S.W. LaFon, B. Sadler, R.E. Walker, J.A. Kovacs, M.A. Polis, R.T. Davey, Jr., H.C. Lane, H. Masur, Atovaquone suspension in HIV-infected volunteers: pharmacokinetics, pharmacodynamics, and TMP-SMX interaction study, Pharmacotherapy, 19 (1999) 1050-1056.
[41] G.L. Nixon, D.M. Moss, A.E. Shone, D.G. Lalloo, N. Fisher, P.M. O'Neill, S.A. Ward, G.A. Biagini, Antimalarial pharmacology and therapeutics of atovaquone, Journal of Antimicrobial Chemotherapy, 68 (2013) 977-985.
[42] R. Dixon, A. Pozniak, H. Watt, P. Rolan, J. Posner, Single-dose and steady-state pharmacokinetics of a novel microfluidized suspension of atovaquone in human immunodeficiency virus-seropositive patients, Antimicrobial agents and chemotherapy, 40 (1996) 556-560.
[43] C.W. Hupple, S. Morscher, N.C. Burton, M.D. Pagel, L.R. McNally, J. Cárdenas-Rodríguez, A light-fluence-independent method for the quantitative analysis of dynamic contrast-enhanced multispectral optoacoustic tomography (DCE MSOT), Photoacoustics, 10 (2018) 54-64.
[44] P. Ghosh, Y. Guo, A. Ashrafi, J. Chen, S. Dey, S. Zhong, J. Liu, J. Campbell, P.C. Konduri, J. Gerberich, M. Garrossian, R.P. Mason, L. Zhang, L. Liu, Oxygen-Enhanced Optoacoustic Tomography Reveals the Effectiveness of Targeting Heme and Oxidative Phosphorylation at Normalizing Tumor Vascular Oxygenation, Cancer Research, 80 (2020) 3542-3555.
[45] M.R. Tomaszewski, I.Q. Gonzalez, J.P. O'Connor, O. Abeyakoon, G.J. Parker, K.J. Williams, F.J. Gilbert, S.E. Bohndiek, Oxygen Enhanced Optoacoustic Tomography (OE-OT) Reveals Vascular Dynamics in Murine Models of Prostate Cancer, Theranostics, 7 (2017) 2900-2913.
[46] M.R. Tomaszewski, M. Gehrung, J. Joseph, I. Quiros-Gonzalez, J.A. Disselhorst, S.E. Bohndiek, Oxygen-Enhanced and Dynamic Contrast-Enhanced Optoacoustic Tomography Provide Surrogate Biomarkers of Tumor Vascular Function, Hypoxia, and Necrosis, Cancer Res, 78 (2018) 5980-5991.
[47] A.V. Silva, U. Norinder, E. Liiv, B. Platzack, M. Öberg, E. Törnqvist, Associations between clinical signs and pathological findings in toxicity testing, Altex, 38 (2021) 198-214.
[48] J. Fillingham, M.-C. Keogh, N.J. Krogan, γ H2AX and its role in DNA double-strand break repair, Biochemistry and cell biology, 84 (2006) 568-577.
[49] S. Goel, D.G. Duda, L. Xu, L.L. Munn, Y. Boucher, D. Fukumura, R.K. Jain, Normalization of the Vasculature for Treatment of Cancer and Other Diseases, Physiological Reviews, 91 (2011) 1071-1121.
[50] M.J.P.S. Kanehisa, Toward understanding the origin and evolution of cellular organisms, 28 (2019) 1947-1951.

Table of Contents

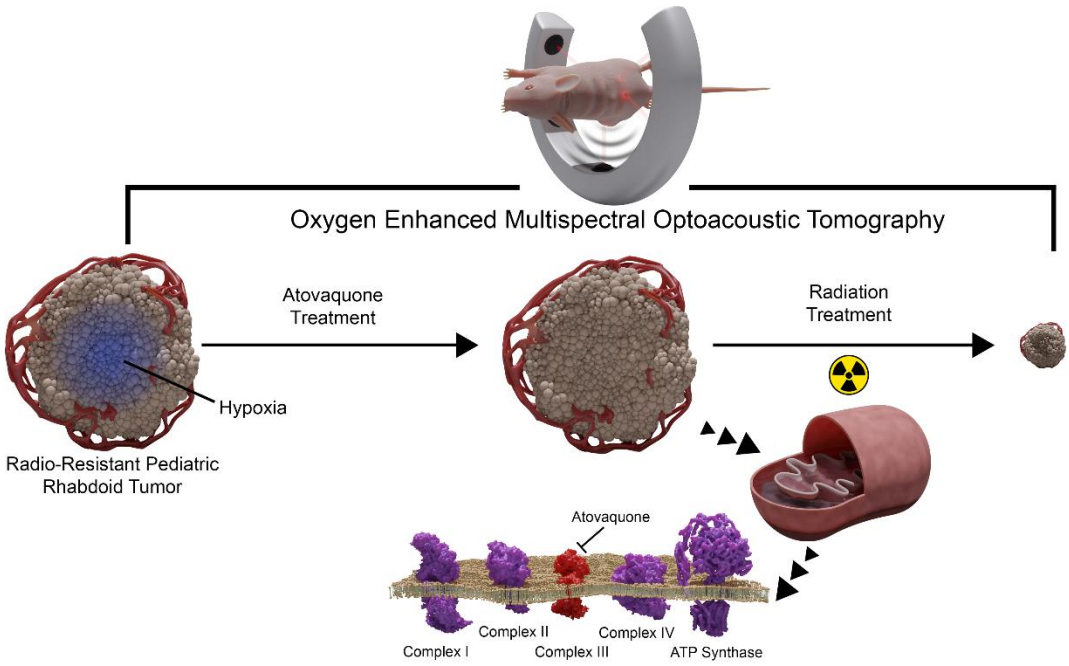

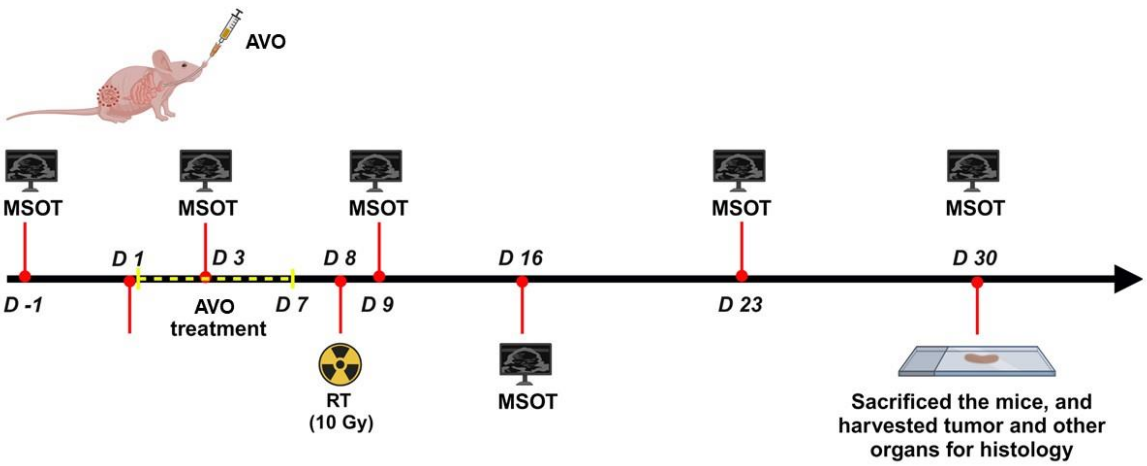

- **Saline group: 7 days saline administration;**
- **AVO treatment group: 7 days AVO administration;**
- **10 Gy treatment group: 7 days saline administration, 10 Gy at D 8;**
- **AVO+10 Gy treatment group: 7 days AVO administration, 10 Gy at D 8.**

Scheme 1: Treatment and imaging plan of A-204 MRT xenografts. Once the tumor volume reached 50 mm^3, MSOT scans were performed before (Day-1), during (Day 3), and after (Day 9, 16, 23 and 30) initiating treatment for all groups. Mice were euthanized when the tumors reached 1000 mm^3, or when moribund or at day 60 post-treatment. Tumors and other organs were harvested for subsequent histology analysis. Created with BioRender.com.

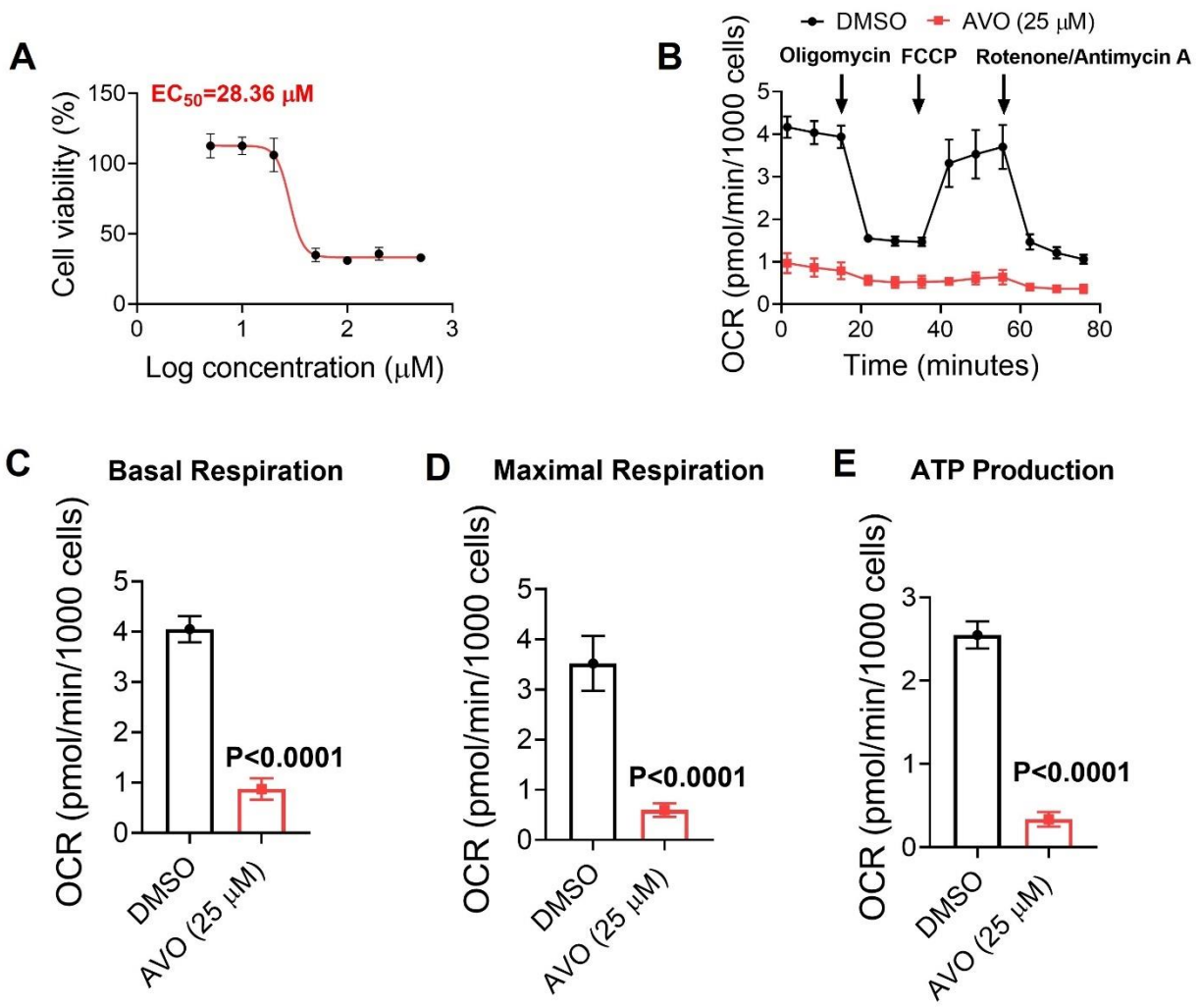

Figure 1: **AVO inhibits mitochondrial respiration of A-204 cells. (A)** Dose response curves depicting the effect of AVO on viability of A-204 cells as tested by MTT assay. Seahorse experiment indicating **(B)** OCR traces of A-204 cells treated with vehicle (DMSO) or AVO. **(C, D, E)** Significant reductions in basal respiration, maximal respiration, and ATP production were observed in AVO treated groups when compared to vehicle-treated controls. All OCR measurements were normalized by Hoechst 33342 staining. Data are presented as mean ± SD.

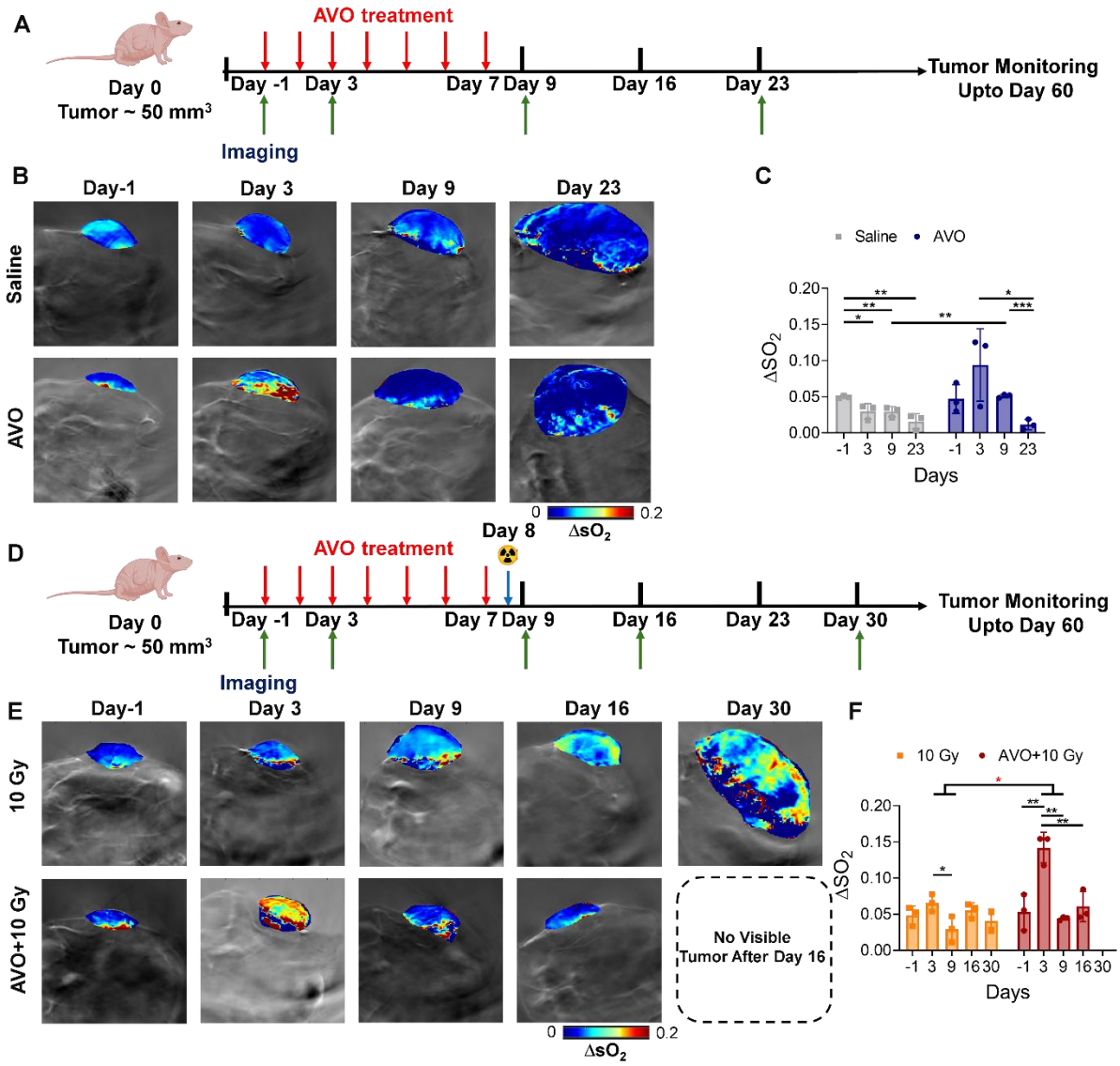

Figure 2: **OE-MSOT shows that AVO treatment improves tumor oxygenation transiently on A-204 xenografts. (A)** Treatment and imaging timeline for saline or AVO-treated groups. (n=3). **(B)** Parametric maps and **(C)** quantitative analysis of tumor ΔsO_2 of saline and AVO treatment groups at each timepoint. **(D)** Treatment and imaging timeline for 10 Gy or AVO+10 Gy-treated groups. (n=3). **(E)** Parametric maps and **(F)** quantification analysis of tumor ΔsO_2 of 10 Gy and AVO+10 Gy treatment groups at each time point. Data are presented as mean ± SD. Statistical analysis as indicated.

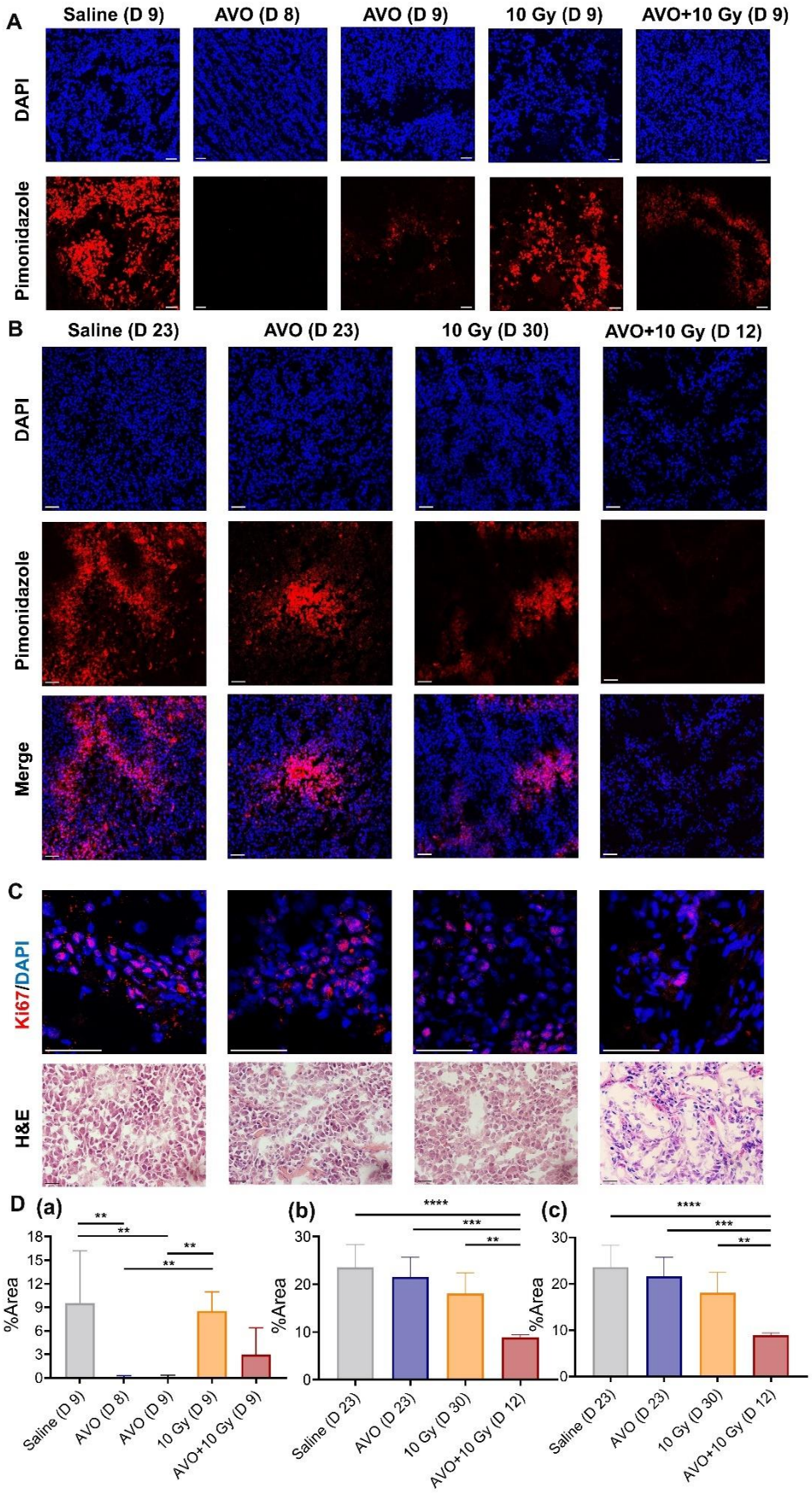
A
Saline (D 9)
AVO (D 8)
AVO (D 9)
10 Gy (D 9)
AVO+10 Gy (D 9)
DAPI
Pimonidazole
B
Saline (D 23)
AVO (D 23)
10 Gy (D 30)
AVO+10 Gy (D 12)
DAPI
Pimonidazole
Merge
C
Ki67/DAPI
H&E
D
(a)
(b)
(c)
%Area
Saline (D 9)
AVO (D 8)
AVO (D 9)
10 Gy (D 9)
AVO+10 Gy (D 9)
Saline (D 23)
AVO (D 23)
10 Gy (D 30)
AVO+10 Gy (D 12)

Figure 3: **Immunofluorescence imaging shows that AVO alleviates tumor hypoxia.** Immunofluorescence imaging of pimonidazole staining of tumors harvested at day 8 and 9 (mid-treatment) **(A)**, and endpoint **(B)** for different treatment groups. **(C)** Ki-67 and H&E staining at endpoint for different groups.. Scale bar = 50 µm. (**D)** Quantitative analysis of pimonidazole at (a: Day 9, b: end point) and Ki-67 at endpoint (c) in all treatment groups. Data are presented as mean ± SD.

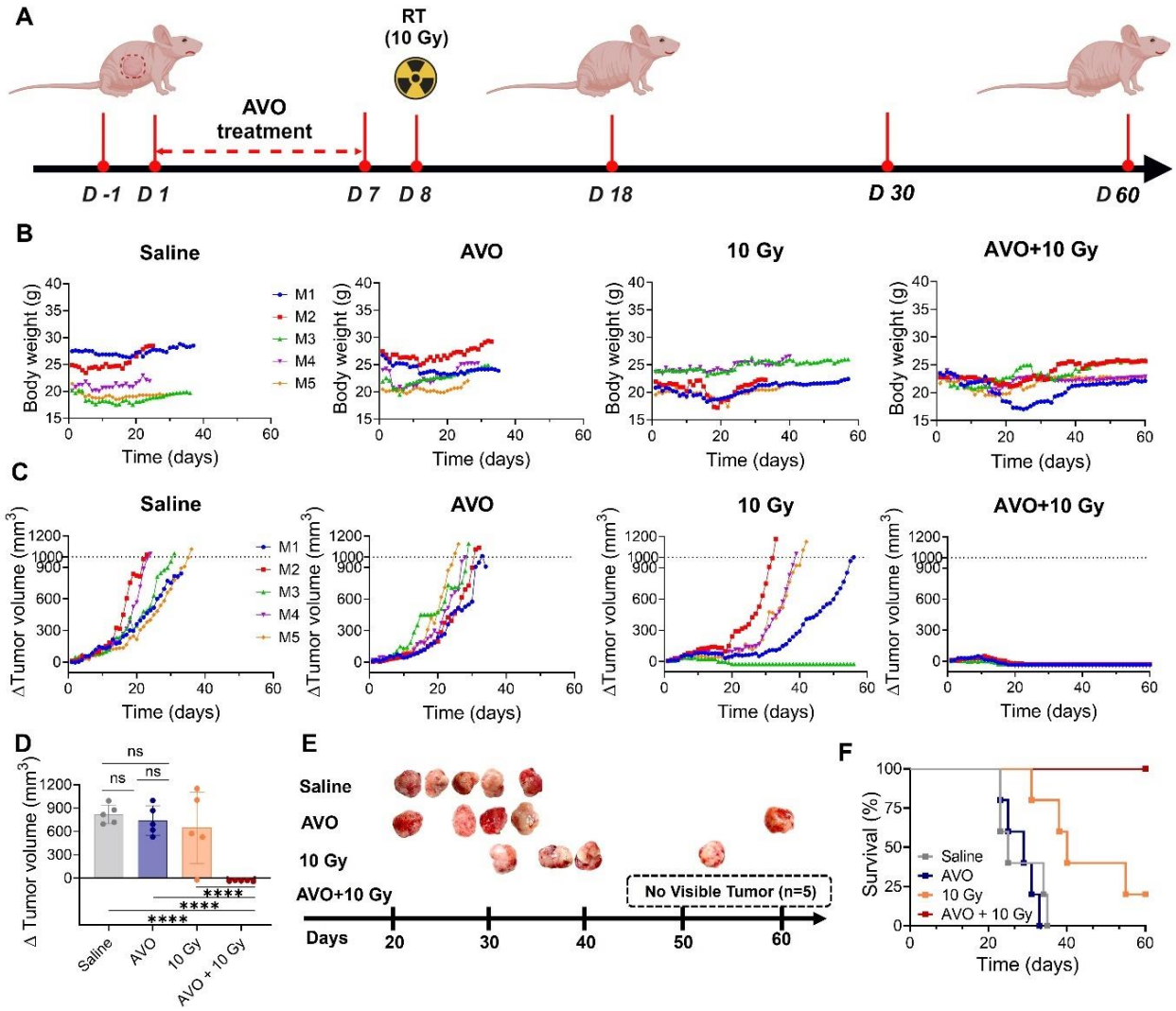

Figure 4: **AVO increases low dose radiation treatment response in A-204 xenografts. (A)** Treatment scheme of AVO+10 Gy combination therapy group. Graphs depicting **(B)** body weight and **(C)** tumor volume changes over 60 days in all treatment groups (n=5). ΔTumor volumes was computed by subtracting tumor volumes at baseline from the tumor volume at each time point. **(D)** ΔTumor volumes and (**E**) Photographs of excised tumors at endpoint for all groups. No visible tumors were found in AVO+10 Gy-treated groups on day 60. (**F**) Kaplan-Meier survival curves forall treatment groups. Data are presented as mean ± SD. Statistical analysis as indicated in the Methods section.

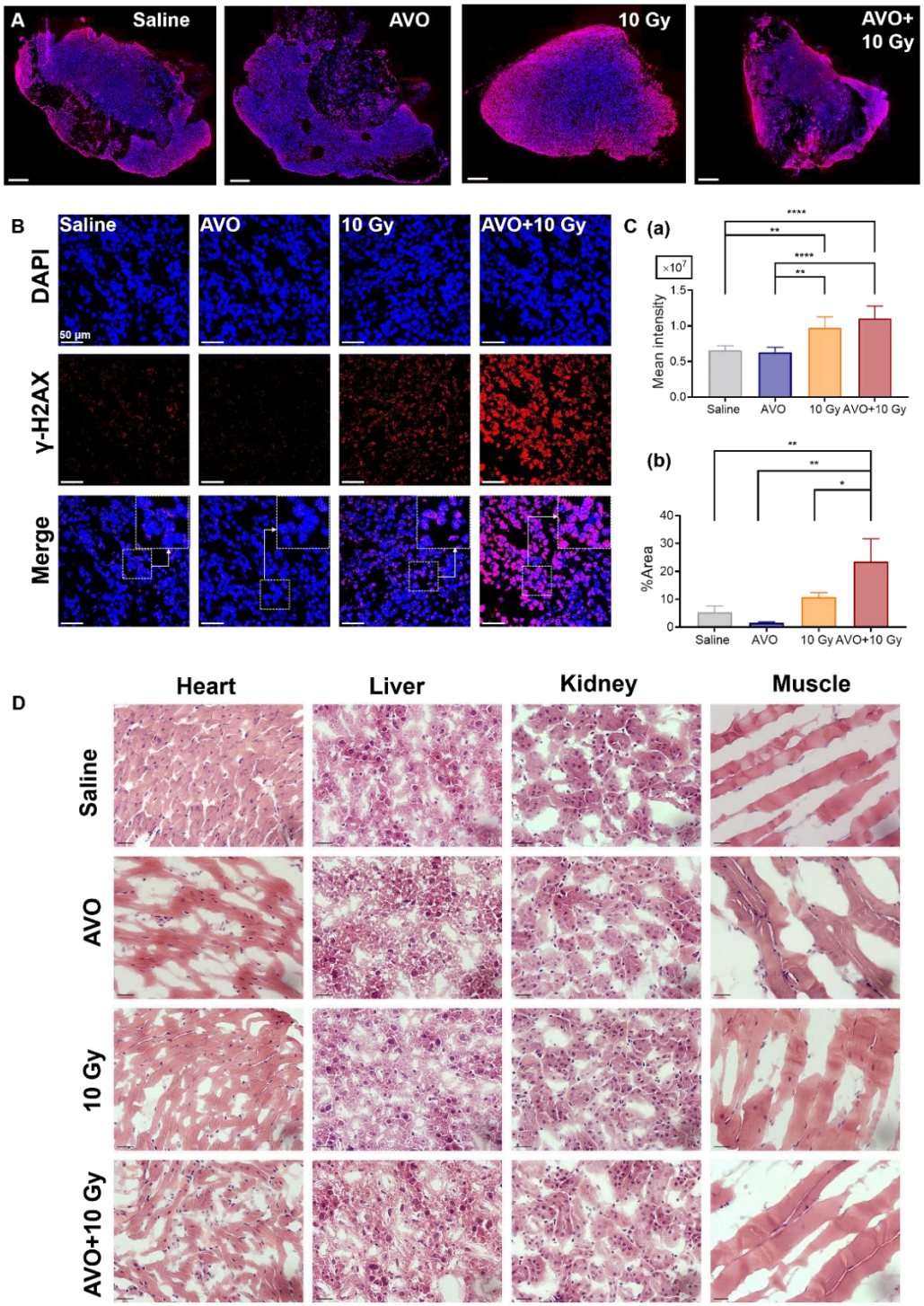

Figure 5: **AVO enhanced DNA damage caused by RT. (A)** Whole tissue imaging and (**B**) confocal micrographs of γ-H2AX immunofluorescence staining of all treatment groups on Day 9. **(Insets)** Stained A-204 tissue at high magnification. Scale bar = 50 µm for confocal images and scale bar = 1000 µm for whole tumor sections. **(C)** Quantification of γ-H2AX staining in whole tumor sections (**a**) and confocal micrographs (**b**) of all treatment groups. **(D)** H&E staining for heart, liver, kidney and muscle from various treatment groups. Scale bar=100 µm. Data represented as mean ± SD.

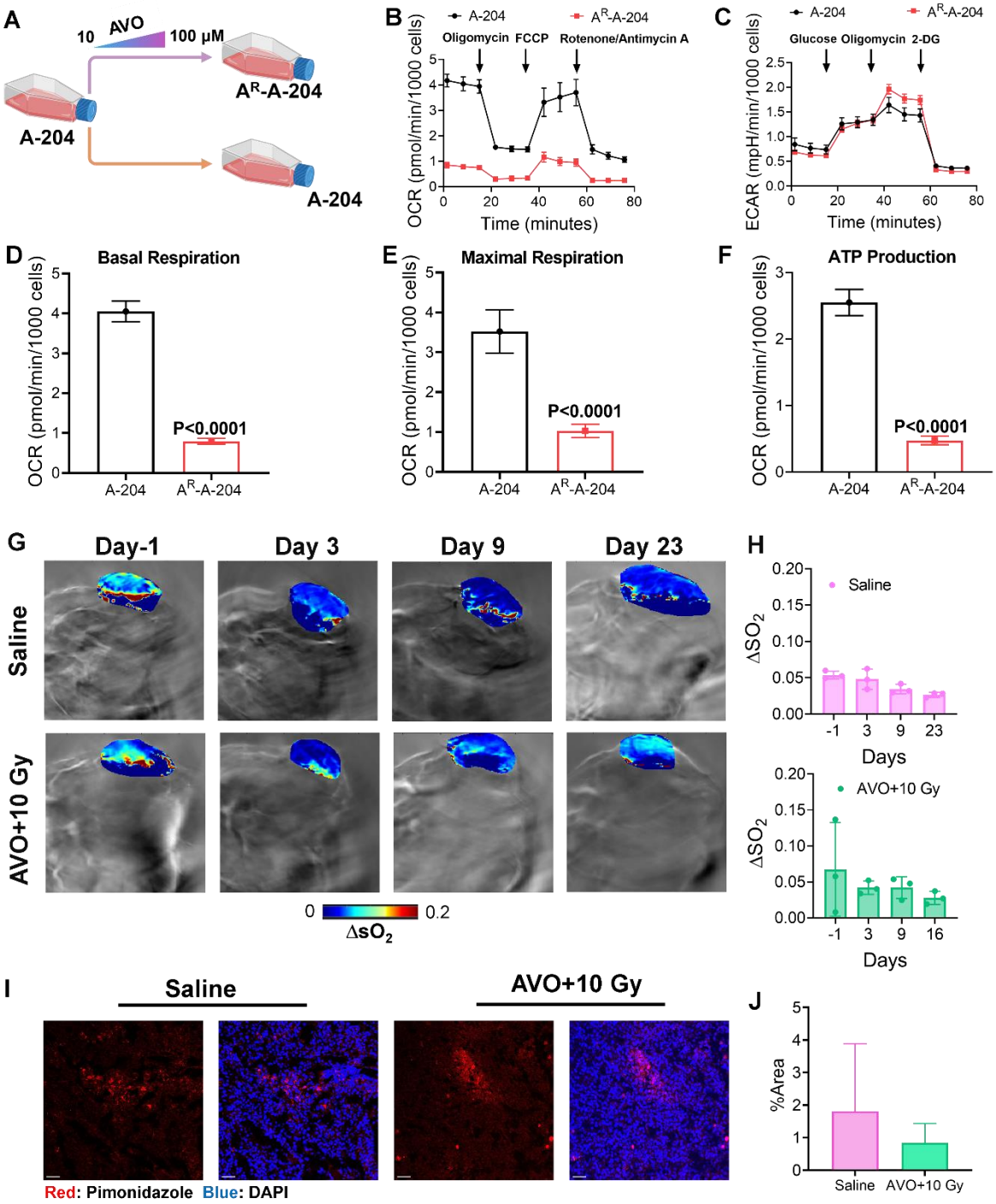

Figure 6: **AVO resistant A^R-A-204 tumors depict altered metabolism and intratumoral hypoxia. (A)** Scheme depicting the generation of AVO-resistant (A^R-A-204) cells. **(B)** OCR and **(C)** ECAR traces of wildtype A-204 and A^R-A-204 cells. **(D, E, F)** Statistically significant reductions in basal respiration, maximal respiration, and ATP production as observed in A^R-A-204 cells when compared to widtypel A-204 cells. **(G)** Parametric maps and **(H)** quantitative analysis of tumor ΔsO_2 for saline and AVO+10 Gy-treated A^R-A-204 xenografts on Day-1, Day 3, Day 9 and Day 23. (n=3). **(I)** Confocal imaging and **(J)** quantitative analysis of pimonidazole staining of excised saline and AVO+10 Gy-treated tumors at endpoint. Scale bar=50 µm.

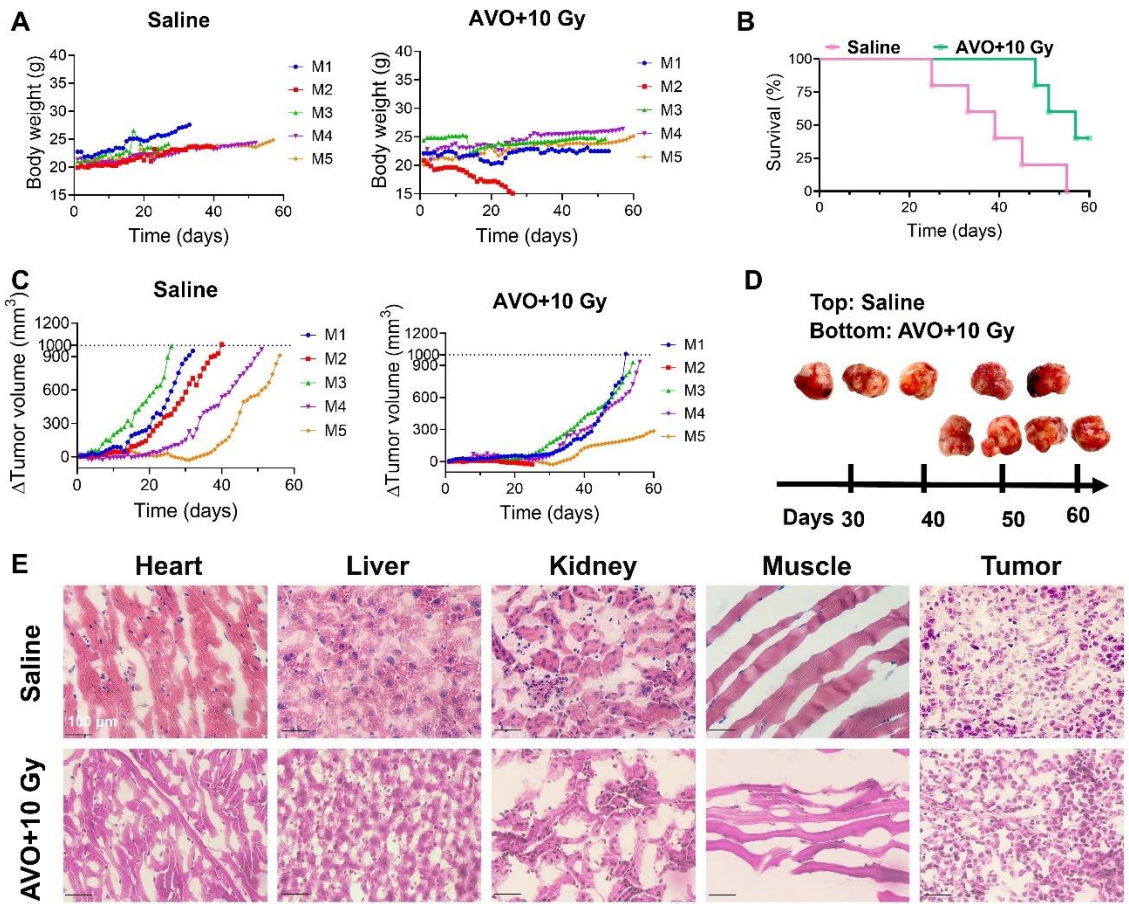

Figure 7: **A^R-A-204 xenografts do not respond to combination therapy. (A)** Body weight curves of saline and AVO+10 Gy-treated groups. **(B)** Kaplan-Meier survival curves and (**C**) individual tumor growth curves depicting change in tumor volume from baseline, for both groups. (**D**) Photographs of excised tumors taken at endpoint. (n = 5) **(E)** H&E staining of heart, liver, kidney, muscle and tumor tissues of each treamtment groups. Scale bar=100 µm.

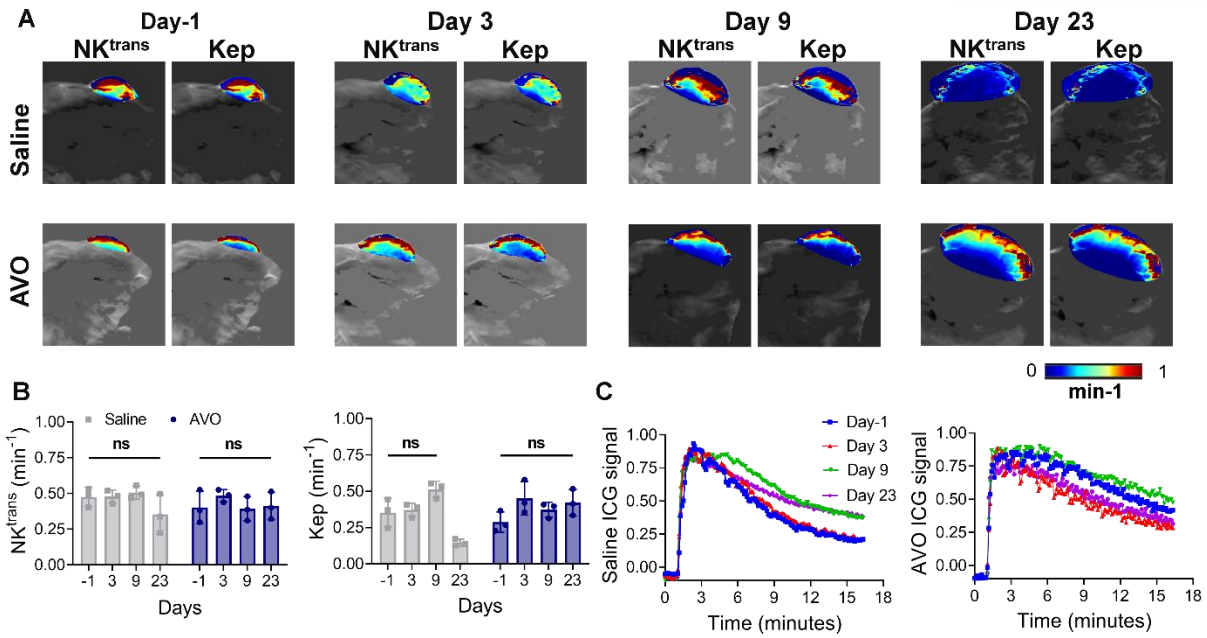

Figure 8: **DCE-MSOT shows that AVO has no impact on tumor perfusion. (A)** Parametric maps and **(B)** quantification analysis of NK^{trans} and K_{ep} for saline and AVO treated A-204 xenografts on Day-1, Day 3, Day 9 and Day 23. (n=3) **(C)** Kinetic curves depicting ICG accumulation in tumors over time in saline and AVO treatment groups. Data presented as mean ± SD.